Performance-optimized diatom-SiO$_x$ anodes for Li-ion batteries by preserving the nanostructured SiO$_2$ shells of diatom microalgae and tailoring oxygen content

Kesavan Thangaian [a],[*], Tove Ericson [b], Per Erik Vullum [c], Pedro Alonso-Sánchez [d], Annlinn Chen Svarverud [a], Ann Mari Svensson [a], Fride Vullum-Bruer [e], Maria Hahlin [b], Maria Valeria Blanco [f]

[a] Department of Materials Science and Engineering, Norwegian University of Science and Technology, Trondheim, Norway
[b] Department of Chemistry Angstrom Laboratory, Uppsala University, Box 538, Uppsala 75121, Sweden
[c] SINTEF Industry, Department of Materials and Nanotechnology, NO 7491, Trondheim, Norway
[d] Aragon Nanoscience and Materials Institute (CSIC - University of Zaragoza) and Physics Condensed Matter Department, C. Pedro Cerbuna 12, 50009 Zaragoza, Spain
[e] SINTEF Energy Research, Department of Thermal Energy, NO 7034, Trondheim, Norway
[f] Institut de Ciència de Materials de Barcelona, ICMAB-CSIC, 08193 Bellaterra, Catalonia, Spain

HIGHLIGHTS

- Nanostructured-SiO$_2$ from cultured diatoms are effective templates for nanoporous SiO$_x$.
- Heat scavenger agents are essential for preserving the nanostructure of diatom-SiO$_2$.
- Tunable oxygen content in SiO$_x$ leads to distinctive electrochemical performance.
- SiO$_x$ anodes with a 1:1:2.5 SiO$_2$:Mg:NaCl ratio deliver superior cycling stability.

GRAPHICAL ABSTRACT
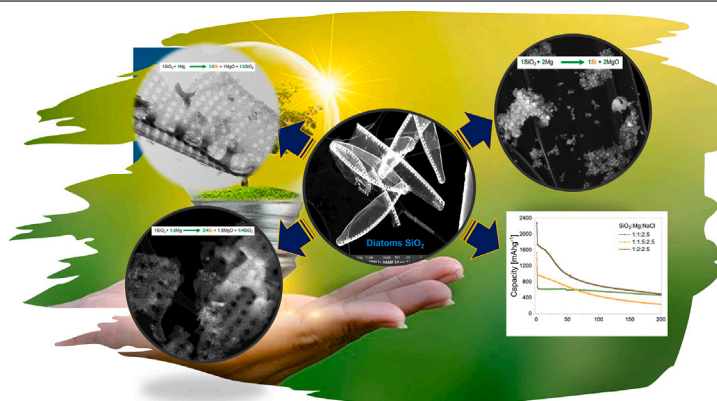
ARTICLE INFO

ABSTRACT

Nanostructured silicon oxides (SiO$_x$) are close-to-market anode materials for increasing the energy density of next-generation lithium-ion batteries (LIBs), offering a balance between high capacity and enhanced cycling stability. However, achieving precise control over SiO$_x$ composition while maintaining structural integrity remains a challenge. In this study, we pioneer the use of nanostructured diatom-SiO$_2$ frustules from industrially cultured Nitzschia sp. microalgae as a sustainable and tunable precursor for high-performance SiO$_x$ anodes via scalable magnesiothermic reduction reaction (MgTR). By optimizing the Mg-to-diatom-SiO$_2$ molar ratio, we demonstrate controlled partial reduction of SiO$_2$, yielding Si nanocrystals embedded within an SiO$_2$ matrix. Notably, we reveal that the preservation of diatom-SiO$_x$ nanoporosity is highly sensitive to reaction exothermic conditions and is effectively stabilized by introducing NaCl as a heat scavenger. Tailoring the reactant

---

* Corresponding author.
E-mail addresses: kesavan.thangaian@ntnu.no (K. Thangaian), vblanco2@icmab.es (M.V. Blanco).

composition (SiO_2:Mg:NaCl = 1:1:2.5) resulted in anodes with superior electrochemical performance, delivering high capacity retention over 200 cycles. Through a comprehensive suite of characterization techniques, we establish the structure–property-performance relationships governing SiO_x anode behavior. These findings mark a major advancement in sustainable SiO_x anode design, providing a scalable strategy for integrating biologically templated nanostructures into high-performance LIBs.

1. Introduction

Graphite has long been the standard anode material for lithium-ion batteries (LIBs) due to its affordability and high cycling stability [1–3]. However, the growing demand for higher energy density LIBs has prompted the exploration of alternative anode materials. Silicon (Si) exhibits a theoretical capacity of 4200 $mAhg^{-1}$, which vastly surpasses graphite's capacity of 372 $mAhg^{-1}$ [4–7], making it a compelling candidate. Nevertheless, its practical application in LIBs faces significant challenges due to the substantial volume changes that occur during lithiation and delithiation, which induce mechanical stress, electrode degradation and rapid capacity fading [8]. To mitigate these issues, strategies such as nanostructuring Si and embedding it within composite matrices have been explored [9–14].

Alternatively, silicon suboxides, SiO_x, consisting of Si and SiO_2 domains, have emerged as promising anode candidates, offering enhanced cycling performance [15–17] along with a specific capacity above 1900 $mAhg^{-1}$. Upon initial lithiation SiO_2 forms Li_xSiO_y, Li_2O and Si, and the silicate phases and lithium oxide are believed to serve as mechanical buffers, stabilizing Si during cycling [18–22]. Despite the improved cycling properties of SiO_x over Si anodes [16], nanostructuring of the material is still essential for achieving long cycling stability. Overall, achieving the full potential of SiO_x anodes relies on the use of sustainable feedstock materials and scalable, cost-effective synthesis techniques that provide control over composition and nanostructure.

Among SiO_x synthesis methods, the magnesiothermic reduction reaction (MgTR) is particularly attractive, as it enables tunable SiO_x compositions at moderate temperatures [23–34], 500 °C and 900 °C, via:

$$SiO_2 + 2Mg \rightarrow Si + 2MgO$$
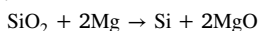
MgO is subsequently removed via acid treatment, leaving a high surface area Si or SiO_x replica. Due to the moderate reaction temperatures, MgTR has shown effectiveness in preserving the nano and microporous framework inherent in the initial SiO_2 template [35]. However, the high exothermic nature of the reaction leads to high localized temperatures [36], causing Si fusion and pore collapse. Heat scavengers, sucg as NaCl (melting point T_m=801 °C) mitigate this effects by absorbing excess heat [37,38], enhancing Si yield and improving reaction control [39–42].

Recent studies have leveraged MgTR to produce Si and SiO_x anodes for LIBs from nanostructured diatomaceous earth (DE) SiO_2 [33,43–46], a fossilized form of diatom frustules that has been previously proposed as anode material [47,48]. DE-SiO_x have shown to achieve reversible capacities of 980 $mAhg^{-1}$ at 100 mAg^{-1} after 100 cycles [43], and 970 $mAhg^{-1}$ after 500 cycles with capacity retention as high as 90% [46]. However, DE-SiO_2 suffers from compositional impurities (85% SiO_2, with a wide range of impurities that vary depending on its origin) and inconsistent morphologies, as DE-SiO_2 is derived from mixtures of different diatom species. This lack of control over composition and morphology limits reproducibility and scalability.

In contrast, industrially cultured single-species diatom microalgae provide a high-purity (97%–98% SiO_2) and morphologically uniform alternative, enabling precise control over structural and chemical properties [49,50]. Also, large-scale, cost-effective cultivation of diatoms presents a cost-effective and sustainable approach for producing SiO_x anode materials. Industrial cultivation techniques, including open-pond systems and photobioreactors, enable high algal productivity, with estimated yields of approximately 70×10^6 t $ha^{-1}year^{-1}$ in open ponds and

about 150×10^6 t $ha^{-1}year^{-1}$ in photobioreactors [51]. Despite these advantages, no study has yet explored MgTR synthesis from cultured diatoms. The nanometer thick, nanoporous SiO_2 network of cultured diatoms poses a significant challenge, as the high exothermic character of MgTR can lead to pore collapse and particle sintering. Therefore, precise control over reactant composition and heat dissipation is essential for producing diatom-SiO_x with preserved nanostructures. Experimental validation is required to assess the feasibility of this approach for next-generation LIBs.

This study pioneers the use of nanostructured diatom-SiO_2 frustules from industrially cultured Nitzschia sp. microalgae as a sustainable and precisely controlled precursor for SiO_x anodes in LIBs. Nitzschia sp. was specifically selected based on its well-defined morphology, which has been shown to enhance electrochemical performance [49]. By systematically tuning the Mg-to-diatom-SiO_2 molar ratio during MgTR, we tailored the stoichiometry and surface properties of SiO_x to optimize its electrochemical behavior. Additionally, we explored the role of NaCl as a heat scavenger to mitigate excessive reaction exothermicity, thereby preserving the intricate nanostructure of the diatom frustules— a critical aspect for long-term cycling stability. Through comprehensive characterization using XRD, TEM/EELS, SEM, XPS, and BET analysis, we establish structure–property-performance relationships that provide valuable insights into the development of high-performance SiO_x anodes. The findings not only validate the feasibility of diatom-derived SiO_x for scalable production but also mark a significant step toward the sustainable fabrication of next-generation LIBs.

2. Experimental

2.1. Synthesis of diatom-SiO_x

Nanostructured diatom-SiO_2 was extracted from the shells of industrially cultured Nitzchia sp. diatom microalgae (Swedish Algae Factory, Sweden). Diatom-SiO_2, Mg powder ($\geq$ 99%, Sigma Aldrich), and NaCl ($\geq$ 99%, Sigma Aldrich) were used as reagents. The powders were mixed in varying molar ratios, according to Table 1, using an agate mortar and transferred to an alumina crucible. The samples were placed in an Ar-filled glovebox and sealed inside a stainless steel (SS) reactor with a graphite gasket. The SS reactor was then heated in a tube furnace at 650 °C for 2 h under an Ar flow, with a ramp rate of 2 °C/min. After annealing, the resulting powders were treated with diluted HCl and stirred overnight to remove impurities such as MgO and Mg_2Si. The materials were subsequently washed thoroughly with deionized water (DI) and ethanol before drying at 60 °C overnight. The complete step-by-step MgTR synthesis process used to produce different diatom-SiO_x materials is illustrated in Fig. 1.

2.2. Materials characterization

Structural analysis of the powder samples was performed by X-ray Diffraction (XRD) using a Bruker D8 A25 DaVinci X-ray Diffractometer with CuKα radiation. N_2 adsorption–desorption isotherms were measured at 77 K using a Tristar 3000 Surface Area and Porosity Analyzer. Prior to the measurements, samples were out-gassed under vacuum at 250 °C overnight.

Diatom-SiO_2 and synthesized diatom-SiO_x powders were analyzed by SEM and TEM. The powders were dispersed in isopropanol, ultrasonicated for ca. 10 min, before a droplet was transferred to an amorphous, lacey carbon coated Cu TEM grid. A Helios 5 PFIB from Thermo Fisher
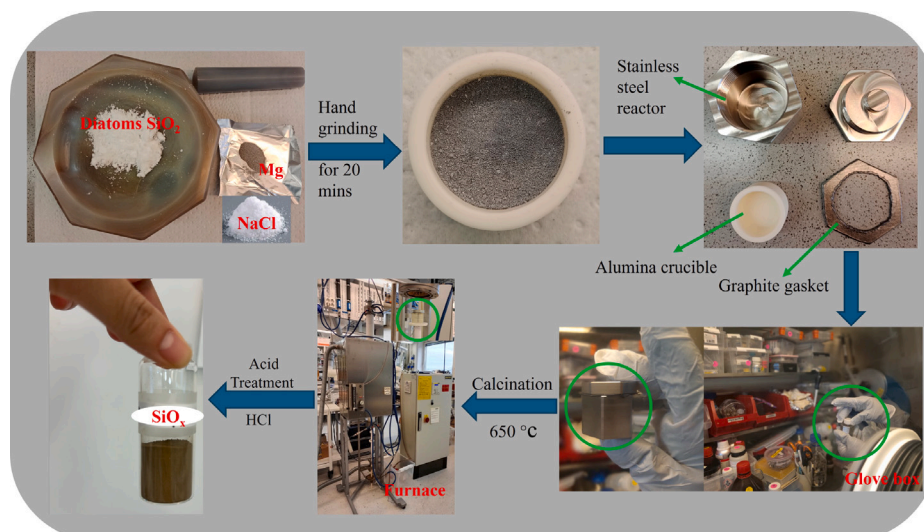
Fig. 1. Step by step schematic illustration for the production of diatom-SiO$_x$ by diatom-SiO$_2$ MgTR.

Table 1
Summary of sample IDs and reactants molar ratios used for diatom-SiO$_2$.

Sample ID	SiO$_2$: Mg : NaCl
SM	1:1
SMN	1:1:5
SMN-1	1:1:2.5
SMN-1.5	1:1.5:2.5
SMN-2	1:2:2.5

was used to acquire high angle annular dark field scanning transmission electron microscopy (HAADF STEM) images at 30 kV. Transmission electron microscopy (TEM) was performed with a double spherical aberration corrected cold field emission gun JEOL ARM 200F, operated at 200 kV. Dual electron energy loss spectroscopy (EELS), using a GIF Quantum ER, and energy dispersive X-ray spectroscopy (EDS), using a 100 mm^2 Centurio detector covering a solid angle of 0.98 sr, were performed simultaneously in STEM mode. Thickness maps of the SiO$_2$ frustules were done by EELS where the log-ratio method was employed to determine the thickness as a function of inelastic mean free paths in every pixel of the map. This relative thickness was converted to absolute thickness in nm by using an inelastic mean free path of 155 nm, as given by Iakoubovskii and Mitsuishi [52]. In EELS, the Si 2p-edge was used to create the Si maps. The energy onset of this edge is sensitive to the oxidation state of silicon, changing from 99 eV for zero-valent Si to 105 eV for fully stoichimetric SiO$_2$. In the diatom-SiO$_x$ powders, Si exists either as pure, zero-valent Si or it remains as amorphous SiO$_2$. The background-subtracted Si 2p-edge in the energy range 99–103 eV was used to map the Si grains, i.e. the part of the Si that was reduced from SiO$_2$ to pure Si.

X-ray photoelectron spectroscopy (XPS) measurements were performed with a Kratos AXIS Supra+ X-ray photoelectron spectrometer using a monochromatic Al Kα X-ray source and an Ag Lα X-ray source. Measurement area was 700x300 µm. The samples were mounted floating and charge neutralization was used. The spectra were fitted with symmetric pseudo-Voigt functions with fixed Lorentzian full-width half-maximum (FWHM) of 0.2 eV and varied Gaussian FWHM. A doublet was used for the Si-Si peak (separation of 0.63 eV, 0.5 difference in height, same FWHM) and a single peak for the Si-O contribution. The fitted Si-O peak was placed at 103.5 eV (expected for SiO$_2$) and Shirley background was used (see also SI Note 1). The X-ray absorption spectroscopy of the Si K-edge was measured with a photodiode detector (AXUV100) at the HIPPIE beamline at MAX IV, Lund, Sweden [53].

2.3. Electrode preparation and characterization

Electrodes were prepared by mixing diatom-SiO$_x$ powder, carbon black (Timcal C-NERGY™ C65) and sodium alginate binder (Sigma Aldrich) in a 50:35:15 mass ratio. The components were homogenized using an horizontal radially oscillating mixer (RETSCH MM400) operating at 25 Hz for 45 min. The resulting slurries were tape casted onto 18 µm thick Cu foil. The electrodes mass loading was of 0.6 mgcm^{-2}. Electrodes were dried under vacuum overnight at 120 °C and then transferred to an Ar-filled glove box for further assembly into coin cells, using lithium foil as the counter electrode and 1 M LiPF$_6$ in 50:50 vol% EC:DEC electrolyte (Sigma Aldrich).

Half-cells were galvanostatically cycled between 2 mV and 2 V versus Li$^+$/Li, at a current density of 100 mAg^{-1}. Rate capability tests were performed at variable currents of 50 mAg^{-1}, 100 mAg^{-1}, 200 mAg^{-1}, 500 mAg^{-1}, 1000 mAg^{-1} and 2000 mAg^{-1} using a Bio-logic potentiostat/galvanostat. All measurements were carried out at a constant temperature of 25 °C.

3. Results and discussion

3.1. Effect of NaCl content on the diatom-SiO$_x$ compounds

Fig. 2a-g present micrographs of diatom-SiO$_2$ shells, used as template material for the synthesis of SiO$_x$ compounds. HAADF images reveal that the diatom-SiO$_2$ structure is about 30 µm in length and about 5 µm in width, characterized by well defined circular pores, Fig. 2a. Notably, HAADF-STEM images at various magnifications, Fig. 2b, Fig. 2c, and Fig. 2d, exhibit uniform SiO$_2$ density, with darker contrast indicating areas of surface or bulk porosity; this contrast is associated with the projected thickness of the frustule. Figs. 2e-g present STEM-EELS-EDS elemental maps, displaying the distribution of Si and O. Additionally, elemental traces of Na, S and Cl were detected in the frustules, as indicated in the EDS spectrum, Fig. S1 of the Supplementary Information (SI). Fig. 2h shows an EELS color map depicting the projected thickness of the frustule. The line profile corresponding to the region beneath the 2 µm white arrow in Fig. 2h is presented in Fig. 2i, revealing that the frustule thickness does not exceed 50 nm.

Fig. 3a shows the XRD patterns of samples *SM*, *SMN* and *SMN-1* synthesized via MgTR from mixtures with a constant diatom-SiO$_2$ to Mg molar ratio of 1:1, and varying NaCl content (0, 2.5 and 5, respectively), according to Table 1. All samples display a broad intensity bump around 2θ=22°, which is characteristic of amorphous SiO$_2$, along
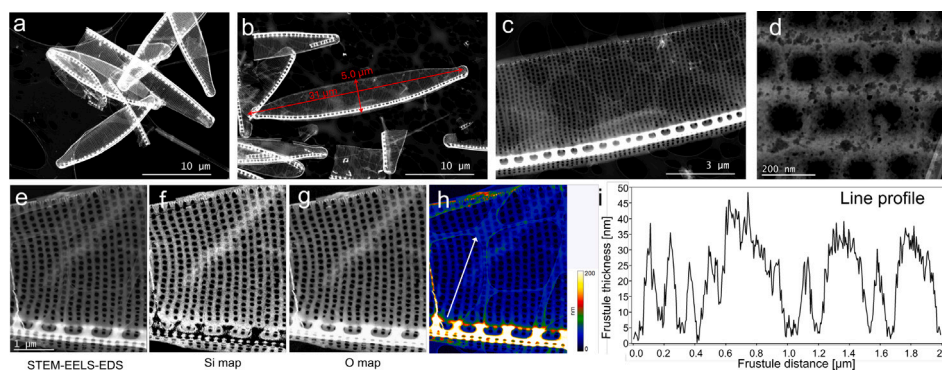
Fig. 2. Diatom-SiO$_2$ frustule: (a-c) HAADF STEM images taken at 30 kV with a Helios 5, (d,e) 200 kV, HAADF STEM images, (f,g) Si and O element maps from STEM-EELS mapping, (h) projected thickness of the mapped region, (i) frustule thickness along the white line in (h).
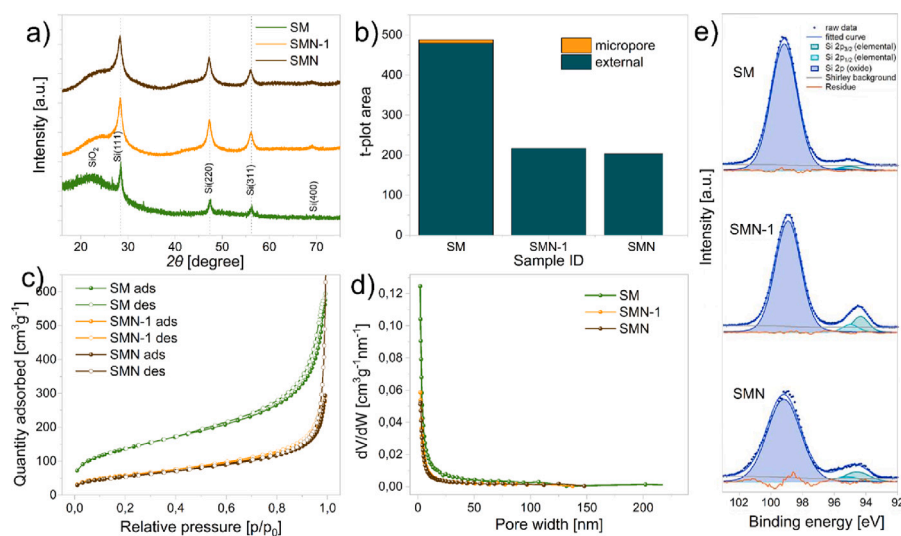

Fig. 3. (a) XRD patterns, (b) BET micropore and external surface area, (c) N$_2$ adsorption–desorption isotherms, (d) pore size distribution plots, (e) Si 2p XPS spectra corresponding to samples without NaCl (*SM*) and with increasing amounts of NaCl (*SMN* and *SMN-1*).

with characteristic crystalline Si reflections (JCPDS Ref. No.: 00-005-0565). No other phases are detected. The calculated lattice parameters of crystalline Si (c-Si) exhibit a clear decreasing trend with increasing NaCl content (Table S1 in SI). In contrast, complementary estimations of the intensity ratio between the amorphous SiO$_2$ hump and c-Si do not show a similarly distinct trend. A significant change is observed upon the addition of NaCl; however, the ratio remains nearly constant between samples containing 2.5 and 5 molar amounts of NaCl (Table S2 in SI). Gas adsorption analysis reveals a surface area of 479 m^{2}g^{-1} for the *SM* sample, which decreases significantly to 217 m^{2}g^{-1} and 203 m^{2}g^{-1} in samples *SMN* and *SMN-1*, respectively. Additionally, only the *SM* sample shows detectable micropore area. This is further supported by the N$_2$ adsorption–desorption isotherms, where the *SM* sample exhibits type IV isotherms, indicative of mesoporous structures, while samples containing NaCl display type II isotherm, characteristic of non-porous or macroporous materials, Fig. 3c. Pore size distribution plots in Fig. 3d also indicate that *SM* exhibit a higher proportion of micropores.

XPS analysis was used to gain further compositional insights. Survey scan analysis revealed that all samples exhibit high purity levels within the information depth of the XPS (nm), although C and small amounts of Na were detected, Fig. S2. Given that a portion of the existing O was found to be bond to carbon, Si to SiO$_2$ ratios could not be easily estimated from quantitative analysis of Si and O spectra. However, using the Si 2p signal it was possible to estimate the ratio of Si bound to Si and Si bound to O. The area ratio of Si-Si to Si-O provides a robust

indication of variations in the Si/SiO$_2$ ratio across different samples (Note S2 in SI). It must however, be considered that XPS results are surface sensitive and that pure Si is expected to react with the oxygen in the air, creating a native oxide of finite thickness, which would result in a non-homogeneous compositional depth profile. Nevertheless, the expected trend in elemental Si to SiO$_2$ is observed for the different samples.

Fig. 3e displays the Si spectra together with the fitted curves. Results of the fitted Si 2p spectra show a Si to SiO$_2$ proportion of 4:96, 12:88 and 12:88 for samples *SM, SMN and SMN-1*, respectively, which is in line with XRD results showing a higher SiO$_2$ proportion for the *SM* sample and higher amounts of Si for samples *SMN* and *SMN-1*. Additional fluorescence yield X-ray absorption spectroscopy (FY XAS) measurements, which has a significantly larger information depth than XPS, was performed for sample *SMN* and results showed a substantially higher Si/SiO$_2$ ratio confirming the non-homogeneous depth profile (Fig. S3 and Note S3 in SI).

Fig. 4 presents bright field micrographs and STEM-EELS-EDS maps of the powder samples. Bright field images of partially reduced SiO$_x$ particles from sample *SM*, Fig. 4a, show a loss of the nanostructured morphology characteristic of the original SiO$_2$ template. Nano-sized Si crystals embedded within an amorphous SiO$_2$ matrix are visible, along with larger crystals exhibiting 111 twinning. By comparing the reduced Si map and the oxygen map (all oxygen in the form of SiO$_2$), it can be observed that nanoscopic, crystalline Si domains are homogeneously dispersed in the SiO$_2$ matrix. In contrast, sample *SMN*, Fig. 4b, retains the nanostructured features of the SiO$_2$ template, suggesting that
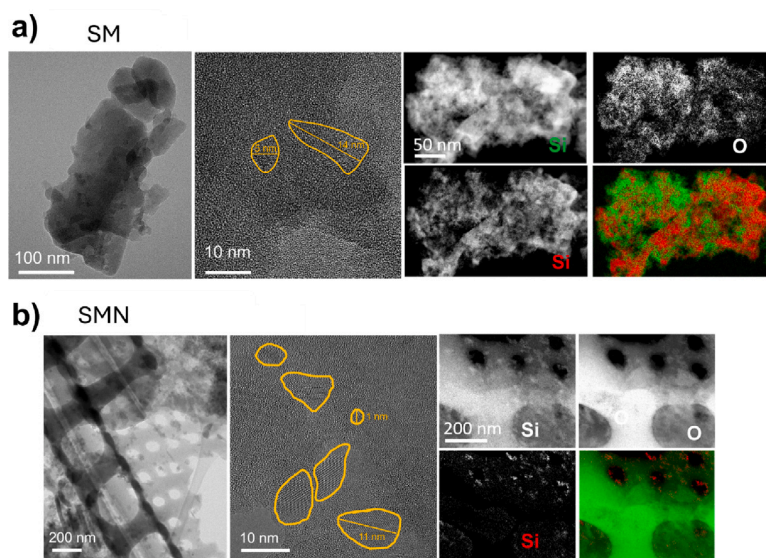
Fig. 4. STEM-EELS-EDS element maps corresponding to: (a) *SM* and (b) *SMN*. The difference between the two Si maps, is that the upper map (green Si label) shows the entire Si signal while the lower map (red Si label) shows only the reduced part of the Si. The color maps combines the oxygen and reduced Si maps. O has green color while the reduced Si has red color. (For interpretation of the references to color in this figure legend, the reader is referred to the web version of this article.)

the presence of NaCl is critical for maintaining particle morphology. Both bright field TEM and EELS maps show multiple crystalline Si nanodomains surrounded by amorphous SiO_2 matrix.

Sample *SM* exhibits a lower Si to SiO_2 ratio, as indicated by XRD and XPS measurements, along with a loss of the SiO_2 template morphology and a higher surface area compared to *SMN* and *SMN-1*. This suggests that reductions conducted without NaCl result in elevated temperatures, leading to the collapse of the nanostructure and less conversion of SiO_2 to Si. Similar observations of particle sintering and morphology loss during MgTR in absence of NaCl have been reported in the synthesis of Si [39,41]. The observation that varying the NaCl content does not significantly affect SiO_x properties indicates that 2.5 molar NaCl are sufficient to buffer temperature fluctuations during diatom-SiO_2 MgTR, with higher NaCl content providing no additional benefit to particle morphology.

The galvanostatic cycling performance of the anodes prepared from the different diatom-SiO_x samples is presented in Fig. 5. Initial lithiation capacities of 1996 mAhg^{-1}, 1525 mAhg^{-1} and 1526 mAhg^{-1} are observed for *SM*, *SMN* and *SMN-1* anodes, respectively. The first cycle irreversible capacity losses are 51%, 44% and 47%, respectively, Fig. 5a. After 10 cycles, delithiation capacities decrease to 998 mAhg^{-1}, 608 mAhg^{-1} and 651 mAhg^{-1} for *SM*, *SMN* and *SMN-1*, respectively. Although *SM* exhibits the highest initial capacity, it also shows the most significant capacity fade. In contrast the *SMN-1* anode shows the best capacity retention. Additional structural and galvanostatic results for samples with higher NaCl content are presented Fig. S4a and Fig. S4b of the Supplementary Information, and confirm that *SMN-1* offers best cycling stability. A slight trend of increasing FWHM of the peaks belonging to crystalline Si domains can be observed in the diffraction data of Fig. S4a, indicating that NaCl addition serves to regulate crystallite size, which might ultimately affect the mechanical stability of the anode after repeated lithiation/delithiation cycles.

3.2. Effect of SiO_2 to Mg ratio on the diatom-SiO_x compounds

Fig. 6a presents the XRD patterns for samples synthesized with increasing Mg content, *SMN-1*, *SMN-1.5* and *SMN-2*. In the case of sample *SMN-1*, a significant intensity bump corresponding to amorphous SiO_2 coexisting with Si Bragg reflections can be observed. An increase in Mg content leads to a noticeable reduction in the amorphous SiO_2 signal and a narrowing of the Si peaks. This trend suggests that
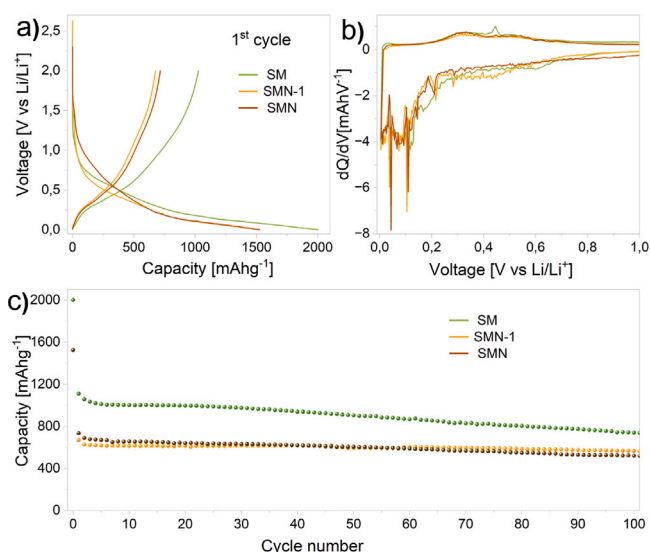

Fig. 5. (a) Voltage profiles of diatom-SiO_x anodes from samples *SM*, *SMN* and *SMN-1*, (b) Corresponding differential capacity plots and (c) Delithiation specific capacity against cycle number during galvanostatic cycling.

higher Mg content enhances the proportion of Si in the synthesized samples and indicates that the heat released during the MgTR of Mg-rich powder mixtures influence the crystallite size of the resulting Si domains. Gas adsorption analysis reveals external surface areas of 216.8 m^{2}g^{-1}, 366.2 m^{2}g^{-1} and 213 m^{2}g^{-1} for *SMN-1*, *SMN-1.5* and *SMN-2* samples, respectively, Fig. 6b. Samples *SMN-1* and *SMN-1.5* exhibit type II N_2 adsorption–desorption isotherms, while sample *SMN-2* shows type IV curves and H3 hysteresis loop, Fig. 6c, indicating the presence of mesopores. Pore size distribution curves also show similar behavior for samples *SMN-1* and *SMN-1.5*, while sample *SMN-2* features more defined pores with a diameter around 12 nm, Fig. 6d. XPS analysis of the Si 2p spectra, Fig. 6e, estimates Si to SiO_2 ratios of 12:88, 41:59 and 58:42 for samples *SMN-1*, *SMN-1.5* and *SMN-2*, respectively, which aligns with the trends observed in the XRD results.

Partially reduced diatom-SiO_2 samples from *SMN-1* and *SMN-1.5* mixtures retain the original nanoporous structure of the SiO_2 frustules,
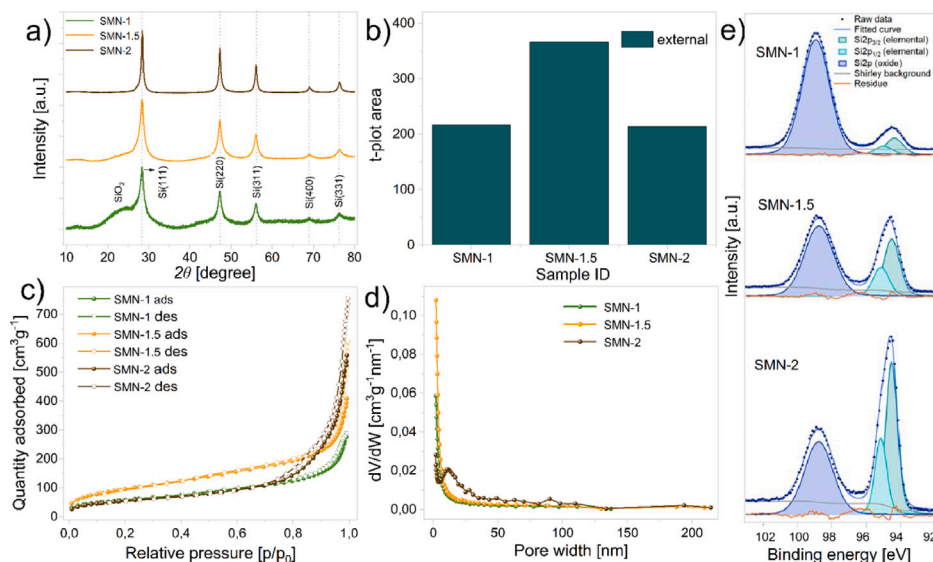
Fig. 6. (a) XRD patterns, (b) BET external surface area, (c) N_2 adsorption–desorption isotherms, (d) pore size distribution plots corresponding to samples having increasing amounts of Mg in the reaction mixtures: *SMN-1*, *SMN-1.5* and *SMN-2*, (e) corresponding XPS Si 2p spectra.

which is indicative of an homogeneous reduction of SiO_2 to Si. This is evidenced in the TEM results by the presence of small Si domains, nanometric in size, evenly distributed throughout the samples, Fig. 7. Inspection of the SEM micrographs reveals the presence of nanoscopic domains at the surface of the particles, which become larger in size when Mg amount is increased in the reactants mixture. By combining SEM, TEM and XRD results it can be suggested that these domains are composed of crystalline Si. The higher number of Si domains in sample *SMN-1.5* can explain the marked increase in the external surface area of this sample compared to sample *SMN-1*. In contrast, sample *SMN-2* exhibits a significant growth of the crystalline Si domains, which is accompanied by the loss of the nanoporous network. This morphological change could explain the drastic decrease in external surface area observed from sample *SMN-1.5* to sample *SMN-2*. Hence, although samples *SMN-1* and *SMN-2* exhibit similar surface areas, the measured areas arise from significantly different morphological characteristics.

These results suggest that the amount of NaCl, used to buffer the temperature increase during the MgTR, of sample *SMN-2* was insufficient to prevent nanopore collapse, probably due to the uncontrolled growth and sintering of multiple small Si nanocrystals into larger crystals. Previous results available in the literature for micron-sized SiO_2 particles, show that lower amounts of NaCl are used for a 1:2 SiO_2 to Mg molar ratio [54]. This indicates that the nanometer thick and nanoporous frustules of diatom-SiO_2 might lead to faster reactions, which may significantly affect heat evolution during the MgTR, leading to collapse of the nanostructure. This indicates that particle morphology has a major effect on MgTR dynamics and that reaction conditions need to be adapted for each system.

Fig. 8 shows electrochemical performance results of the SiO_x anodes. The electrodes exhibit initial lithiation specific capacities of 1525 mAhg^{-1}, 1520 mAhg^{-1} and 2280 mAhg^{-1} for *SMN-1*, *SMN-1.5*, and *SMN-2*, respectively, with irreversible capacity losses of 73.9%, 60.01% and 44.26%, Fig. 8a. Differential capacity plots of the initial and second cycles, Fig. 8c and Fig. 8d, respectively, reveal the presence of cathodic and anodic peaks typical of Si alloying-dealloying reactions across all samples, with more pronounced peaks for the samples prepared with increasing Mg content, as expected. Galvanostatic cycling results, Fig. 8e, indicate a significantly higher specific capacity for sample *SMN-2* over the first 100 cycles, although this is accompanied by a dramatic capacity loss upon further cycling. Sample *SMN-1.5* displays lower initial capacity and follows a similar capacity loss trend as the previous sample. On the other hand, sample *SMN-1*, which displays significantly lower specific capacity, exhibits more stable cycling

Table 2
Summary of sample IDs and specific delithiation capacities, in mAhg^{-1}, at different cycle numbers.

Sample ID/Cycle number	1	10	50	100	200
SMN-1	1525	615	595	568	462
SMN-1.5	1520	927	675	441	238
SMN-2	2280	1643	979	707	497

performance, thus having the same specific capacity as sample *SMN-2* after 200 cycles, Fig. 8e. A summary of delithiation capacity values for different cycle numbers is displayed in Table 2. The results indicate that the Si in *SMN-2* behaves more like a pure Si-based anode rather than a SiO_x-based anode, with the Si particles and surfaces directly exposed to the electrolyte. Due to the significant volume expansions and contractions during electrochemical cycling, the SEI would repeatedly break, exposing fresh Si surfaces to the electrolyte. Additionally, the Si particles likely undergo morphological transformations; initially smooth Si crystals evolve into filigree structures where a network of Si-based nanowires stick out. These morphological changes would increase the overall Si surface area with cycling, leading to a steady increase of new SEI with each cycle. In contrast, in *SMN-1*, a large percentage of the Si crystals would be protected by the SiO_2 matrix, preventing direct contact with the electrolyte. Consequently, a more a stable SEI would be formed on the surface of the SiO_x matrix, while the smaller Si domains within the SiO_2 matrix can (de)lithiate without additional SEI formation. Rate capability tests conducted on the three samples, Fig. 8f, show a similar trend, in which sample *SMN-1* displays the lowest specific capacity for almost all currents, but stable values when decreasing and increasing the current. Sample *SMN-2* displays higher specific capacity at all rates, although it is not able to maintain capacity values when the current is decreased again.

4. Conclusions

In this study, diatom-SiO_x materials characterized by its nanoporous and nanometric structure sourced from industrially cultured single species diatom-SiO_2 were synthesized for the first time through a magnesiothermic reduction reaction, and the effect of using different NaCl content and different Mg content on the reagents mixtures were analyzed independently.

A thorough structural, compositional and morphological analysis on diatom-SiO_x powders synthesized with a fixed 1:1 diatom-SiO_2 to Mg
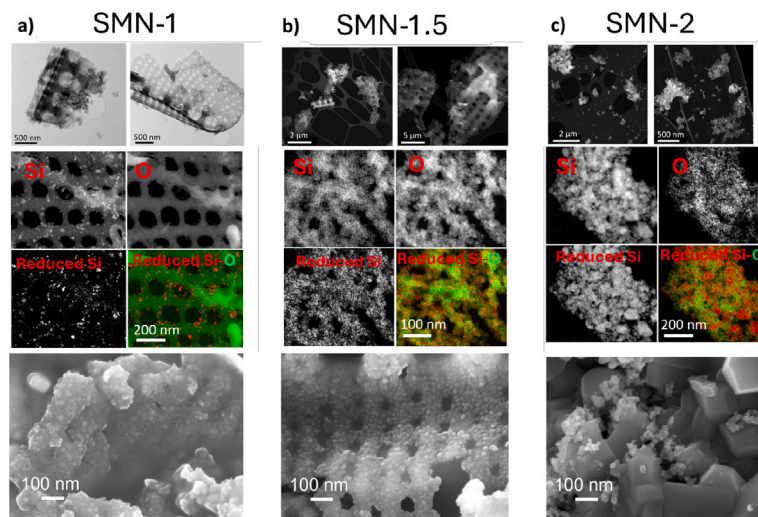
Fig. 7. Top section: bright field TEM images/HAADF STEM images. Middle section: EELS individual chemical maps based on the Si 2p- and O K-edges in the EEL spectra. The maps labeled "reduced Si" show the background subtracted Si 2p signal in the energy range 99 - 103 eV. Therefore, these maps show the reduced, crystalline Si particles. Bottom section: SEM micrographs. (a) *SMN-1*, (b) *SMN-1.5*, and (c) *SMN-2* samples.
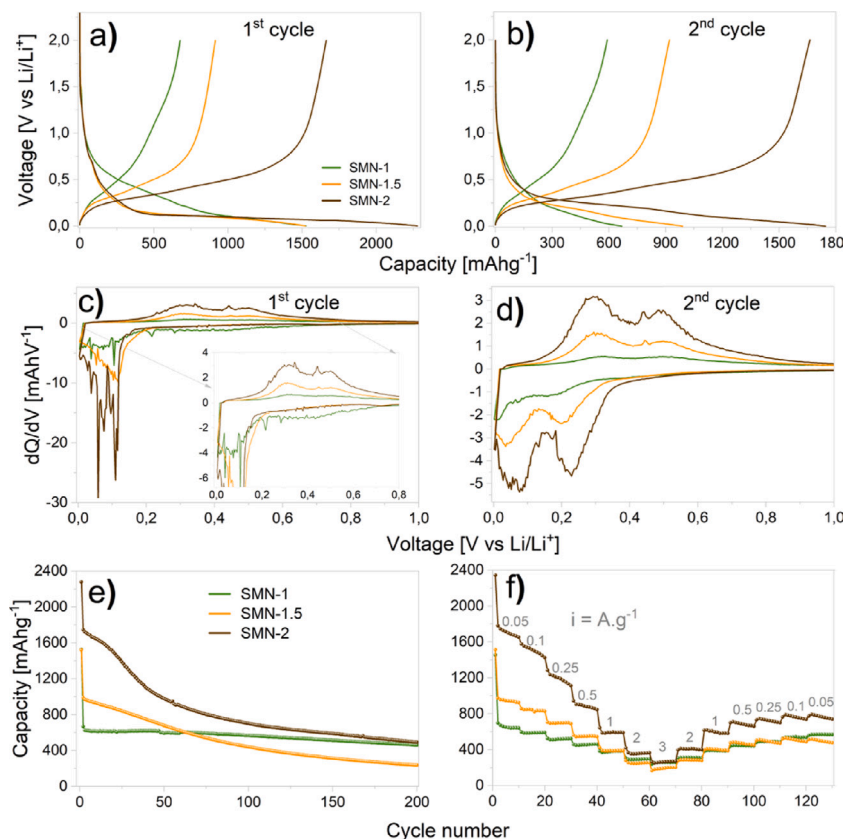

Fig. 8. Voltage profile curves corresponding to (a) first (de)lithiation cycle, (b) second (de)lithiation cycle, (c) first (de)lithiation cycle differential capacity plots, (d) second (de)lithiation cycle differential capacity plots, (e) evolution of specific capacity against cycle number, (f) specific capacity at variable current rates of *SMN-1*, *SMN-1.5* and *SMN-2* anodes.

molar ratio and with 0, 2.5 and 5 molar amounts of NaCl revealed a high sensitivity of the nanoporous and nanometer thick diatom-SiO_2 frustules to MgTR, as the absence of NaCl caused the collapse of the original nanostructure and less conversion of SiO_2 to Si. Adding 2.5 molar amount of NaCl was found to be effective for preserving particle morphology when diatom-SiO_2 to Mg molar ratio was 1:1. An increase of NaCl from 2.5 to 5 had a slight impact on the FWHM of Si reflections,

indicating that samples were exposed to slightly different temperatures during the reduction process. Electrochemical performance of the resulting anodes indicated that samples synthesized in the absence of NaCl exhibited lower capacity retention, whereas higher capacity retention was found for the sample synthesized in the presence of 2.5 molar NaCl. This was attributed to the preservation of the nanoporous structure of the frustule and to an adequate size of Si crystallites,

which would favor allow lithiation/delithiation reactions to proceed reversibly without destabilizing the electrode structure.

Analysis on the variation of diatom-SiO₂ to Mg molar ratios while keeping the NaCl content constant, was also performed. Samples containing diatom-SiO₂ to Mg to NaCl ratios of 1:1:2.5, 1:1.5:2.5 and 1:2:2.5 were synthesized and all samples showed the growth of nanoscopic Si domains evenly distributed in the amorphous SiO₂ matrix of diatom frustules, and such domains became notably larger with increasing amounts of Mg, until SiO₂ to Mg ratio of 1:2, where all the SiO₂ converted into Si. This was accompanied by a narrowing of Si reflections in XRD patterns as the Mg content was increased. BET results showed a significant increase of external surface area when diatom-SiO₂ to Mg ratio was increased from 1:1 to 1:1.5 and attributed to the formation of larger Si domains. The sudden drop of surface area when Mg content was further increased to a 1:2 molar ratio was attributed to nanostructure collapse, which was confirmed by TEM and SEM inspections. Diatom-SiO$_x$ electrodes showed lower irreversible capacity loss on the first cycle for SiO$_x$ samples containing increasing amounts of Si, with values of 44.3%, 60% and 72.3% for electrodes made from 1:1, 1:5 and 1:2 SiO₂:Mg mixtures, respectively. The similar areal properties observed for the 1:1 and 1:2 samples indicate that differences in electrochemical capacity can be attributed to compositional changes and having Si domains embedded in a SiO₂ matrix results in significantly higher capacity retention, whereas large Si crystals in contact with each other and in direct contact with the electrolyte would result in drastic capacity fade. These findings underscores the potential of utilizing sustainable diatom-SiO₂ feedstock to produce high-performance anode materials for Li-ion batteries, with implications for future advancements in battery technology.

CRediT authorship contribution statement

Kesavan Thangaian: Writing – review & editing, Writing – original draft, Validation, Methodology, Investigation, Formal analysis, Data curation, Conceptualization. **Tove Ericson:** Writing – review & editing, Investigation, Formal analysis, Data curation. **Per Erik Vullum:** Writing – review & editing, Validation, Investigation, Formal analysis, Data curation. **Pedro Alonso-Sánchez:** Writing – review & editing, Investigation, Formal analysis, Data curation. **Annlinn Chen Svarverud:** Formal analysis, Data curation. **Ann Mari Svensson:** Writing – review & editing, Validation. **Fride Vullum-Bruer:** Writing – review & editing, Validation, Investigation. **Maria Hahlin:** Writing – review & editing, Validation. **Maria Valeria Blanco:** Writing – review & editing, Writing – original draft, Validation, Supervision, Project administration, Investigation, Conceptualization.

Declaration of competing interest

The authors declare that they have no known competing financial interests or personal relationships that could have appeared to influence the work reported in this paper.

Acknowledgments

Appendix A. Supplementary data

Supplementary material related to this article can be found online at https://doi.org/10.1016/j.jpowsour.2025.236837.

Data availability

No data was used for the research described in the article.

References

[1] R. Fong, U.v. Sacken, J.R. Dahn, J. Electrochem. Soc. 137 (7) (1990) 2009.
[2] R. Yazami, P. Touzain, J. Power Sources 9 (3) (1983) 365–371.
[3] J.R. Dahn, A.K. Sleigh, H. Shi, J.N. Reimers, Q. Zhong, B.M. Way, Electrochim. Acta 38 (9) (1993) 1179–1191.
[4] B. Zhu, X. Wang, P. Yao, J. Li, J. Zhu, Chem. Sci. 10 (30) (2019) 7132–7148.
[5] Y. Qi, G. Wang, S. Li, T. Liu, J. Qiu, H. Li, Chem. Eng. J. 397 (2020) 125380.
[6] A. Casimir, H. Zhang, O. Ogoke, J.C. Amine, J. Lu, G. Wu, Nano Energy 27 (2016) 359–376.
[7] U. Kasavajjula, C. Wang, A.J. Appleby, J. Power Sources 163 (2) (2007) 1003–1039.
[8] G. Zhu, D. Chao, W. Xu, M. Wu, H. Zhang, ACS Nano 15 (10) (2021) 15567–15593.
[9] L. Sun, J. Xie, Z. Jin, Energy Technol. 7 (11) (2019) 1900962.
[10] J.R. Szczech, S. Jin, Energy & Environ. Sci. 4 (1) (2010) 56–72.
[11] J. Tao, L. Lu, B. Wu, X. Fan, Y. Yang, J. Li, Y. Lin, Y.Y. Li, Z. Huang, J. Lu, Energy Storage Mater. 29 (2020) 367–376.
[12] Z. Liu, D. Lu, W. Wang, L. Yue, J. Zhu, L. Zhao, H. Zheng, J. Wang, Y. Li, ACS Nano 16 (3) (2022) 4642–4653.
[13] L. Zhang, C. Wang, Y. Dou, N. Cheng, D. Cui, Y. Du, P. Liu, M. Al-Mamun, S. Zhang, H. Zhao, Angew. Chem. Int. Ed. 58 (26) (2019) 8824–8828.
[14] R. Malik, M.J. Loveridge, L.J. Williams, Q. Huang, G. West, P.R. Shearing, R. Bhagat, R.I. Walton, Chem. Mater. 31 (11) (2019) 4156–4165.
[15] T. Chen, J. Wu, Q. Zhang, X. Su, J. Power Sources 363 (2017) 126–144.
[16] X. Zhu, B. Liu, J. Shao, Q. Zhang, Y. Wan, C. Zhong, J. Lu, Adv. Funct. Mater. 33 (17) (2023) 2213363.
[17] H. Li, H. Li, Z. Yang, L. Yang, J. Gong, Y. Liu, G. Wang, Z. Zheng, B. Zhong, Y. Song, Y. Zhong, Z. Wu, X. Guo, Small 17 (51) (2021) 2102641.
[18] S.C. Jung, H.-J. Kim, J.-H. Kim, Y.-K. Han, J. Phys. Chem. C 120 (2) (2016) 886–892.
[19] Y. Yamada, Y. Iriyama, T. Abe, Z. Ogumi, J. Electrochem. Soc. 157 (1) (2009) A26.
[20] Y. Nagao, H. Sakaguchi, H. Honda, T. Fukunaga, T. Esaka, J. Electrochem. Soc. 151 (10) (2004) A1572.
[21] Z. Liu, Q. Yu, Y. Zhao, R. He, M. Xu, S. Feng, S. Li, L. Zhou, L. Mai, Chem. Soc. Rev. 48 (1) (2019) 285–309.
[22] Y. Zhang, G. Guo, C. Chen, Y. Jiao, T. Li, X. Chen, Y. Yang, D. Yang, A. Dong, J. Power Sources 426 (2019) 116–123.
[23] P. Alonso Sánchez, K. Thangaian, O.A. Øie, A. Gaarud, M. Rodríguez Gomez, V. Diadkin, J. Campo, F.H. Cova, M.V. Blanco, ACS Appl. Energy Mater. 8 (4) (2025) 2249–2259.
[24] L. Su, J. Xie, Y. Xu, L. Wang, Y. Wang, M. Ren, J. Alloys Compd. 663 (2016) 524–530.
[25] J. Song, S. Guo, L. Kou, K. Kajiyoshi, J. Su, W. Huang, Y. Li, P. Zheng, Vacuum 186 (2021) 110044.
[26] Y. Liu, J. Ruan, F. Liu, Y. Fan, P. Wang, J. Alloys Compd. 802 (2019) 704–711.
[27] P. Lv, H. Zhao, C. Gao, T. Zhang, X. Liu, Electrochim. Acta 152 (2015) 345–351.
[28] Y. Ren, M. Li, J. Power Sources 306 (2016) 459–466.
[29] Q. Xu, J.-K. Sun, Y.-X. Yin, Y.-G. Guo, Adv. Funct. Mater. 28 (8) (2018) 1705235.
[30] B.-C. Yu, Y. Hwa, J.-H. Kim, H.-J. Sohn, Electrochim. Acta 117 (2014) 426–430.
[31] J. Ge, Q. Tang, H. Shen, F. Zhou, H. Zhou, W. Yang, J. Hong, B. Xu, J. Saddique, Appl. Surf. Sci. 552 (2021) 149446.
[32] C. Zhou, J. Liu, X. Gong, Z. Wang, J. Alloys Compd. 874 (2021) 159914.
[33] Z. Bao, M.R. Weatherspoon, S. Shian, Y. Cai, P.D. Graham, S.M. Allan, G. Ahmad, M.B. Dickerson, B.C. Church, Z. Kang, H.W. Abernathy III, C.J. Summers, M. Liu, K.H. Sandhage, Nature 446 (7132) (2007) 172–175.
[34] J. Entwistle, A. Rennie, S. Patwardhan, J. Mater. Chem. A 6 (38) (2018) 18344–18356.
[35] E.K. Richman, C.B. Kang, T. Brezesinski, S.H. Tolbert, Nano Lett. 8 (9) (2008) 3075–3079.
[36] C.W. Won, H.H. Nersisyan, H.I. Won, Sol. Energy Mater. Sol. Cells 95 (2) (2011) 745–750.
[37] X. Wan, Z. Tang, J. Chen, Y. Xue, J. Zhang, X. Guo, Y. Liu, Q. Kong, A. Yuan, H. Fan, Chem. Lett. 48 (12) (2019) 1547–1550.
[38] P. Han, W. Sun, D. Li, D. Luo, Y. Wang, B. Yang, C. Li, Y. Zhao, L. Chen, J. Xu, C. Zhu, Appl. Surf. Sci. 481 (2019) 933–939.
[39] R. Miao, S. Kang, W. Liao, Y. Wang, J. Liu, G. Zhong, H. Wu, J. Zhang, Ionics 26 (3) (2020) 1249–1259.

[40] Z. Favors, W. Wang, H.H. Bay, Z. Mutlu, K. Ahmed, C. Liu, M. Ozkan, C.S. Ozkan, Sci. Rep. 4 (1) (2014) 5623.

[41] A. Ansari Hamedani, C.W. Ow-Yang, S. Hayat Soytas, ChemElectroChem 8 (16) (2021) 3181–3191.

[42] S.H. Lee, Y. Cho, Y.P. Jeon, Y. Chang, K.S. Lee, D. Hong, O.S. Jeon, Y. Park, H.S. Yang, Y.J. Yoo, S.Y. Park, Y. Piao, EcoMat 5 (11) (2023) e12401.

[43] H. Ruan, S. Guo, L. Zhang, Y. Liu, L. Li, Y. Huang, S. Gao, Y. Tian, Ceram. Int. 48 (12) (2022) 17510–17517.

[44] L.-f. Guo, S.-y. Zhang, J. Xie, D. Zhen, Y. Jin, K.-y. Wan, D.-g. Zhuang, W.-q. Zheng, X.-b. Zhao, Int. J. Miner. Met. Mater. 27 (4) (2020) 515–525.

[45] M. Cui, L. Wang, X. Guo, E. Wang, Y. Yang, T. Wu, D. He, S. Liu, H. Yu, J. Mater. Chem. A 7 (8) (2019) 3874–3881.

[46] Y. Zhang, R. Zhang, S. Chen, H. Gao, M. Li, X. Song, H.L. Xin, Z. Chen, Adv. Funct. Mater. 30 (50) (2020) 2005956.

[47] M.V. Blanco, V. Renman, F. Vullum-Bruer, A.M. Svensson, RSC Adv. 10 (55) (2020) 33490–33498.

[48] W. Hua, I.-E. Nylund, F. Cova, A.M. Svensson, M.V. Blanco, Sci. Rep. 13 (1) (2023) 20447.

[49] K. Thangaian, W. Hua, J.T. Aga Karlsen, I.-E. Nylund, S. Nilsson, T. Ericson, M. Hahlin, A.M. Svensson, M.V. Blanco, ACS Sustain. Resour. Manag. 1 (4) (2024) 767–777.

[50] K. Thangaian, A. Gaarud, I.-E. Nylund, M.V. Blanco, ACS Sustain. Resour. Manag. (2024).

[51] I. Rea, M. Terracciano, L. De Stefano, Adv. Heal. Mater. 6 (3) (2017) 1601125.

[52] K. Iakoubovskii, K. Mitsuishi, Y. Nakayama, K. Furuya, Phys. Rev. B 77 (10) (2008) 104102.

[53] S. Zhu, M. Scardamaglia, J. Kundsen, R. Sankari, H. Tarawneh, R. Temperton, L. Pickworth, F. Cavalca, C. Wang, H. Tissot, J. Weissenrieder, B. Hagman, J. Gustafson, S. Kaya, F. Lindgren, I. Källquist, J. Maibach, M. Hahlin, V. Boix, T. Gallo, F. Rehman, G. D'Acunto, J. Schnadt, A. Shavorskiy, Journal Synchrotron Radiation 28 (2) (2021) 624–636.

[54] A. Darghouth, S. Aouida, B. Bessais, Silicon 13 (3) (2021) 667–676.